LOW-DIMENSIONAL SYSTEMS

Properties of the Amorphous–Nanocrystalline Gd₂O₃ Powder Prepared by Pulsed Electron Beam Evaporation

V. G. Il'ves[a], *, S. Yu. Sokovnin[a, b], S. A. Uporov[c], and M. G. Zuev[b, d]

[a] *Institute of Electrophysics, Ural Branch of the Russian Academy of Sciences,*
ul. Amundsena 106, Yekaterinburg, 620216 Russia

* e-mail: ilves@iep.uran.ru

[b] *Ural Federal University named after the First President of Russia B. N. Yeltsin*
(on the basis of Ural State Technical University–UPI), ul. Mira 19, Yekaterinburg, 620002 Russia

[c] *Institute of Metallurgy, Ural Branch of the Russian Academy of Sciences,*
ul. Amundsena 101, Yekaterinburg, 620016 Russia

[d] *Institute of Solid State Chemistry, Ural Branch of the Russian Academy of Sciences,*
ul. Pervomaiskaya 91, Yekaterinburg, 620990 Russia

Received November 7, 2012

Abstract—An amorphous–nanocrystalline Gd_2O_3 powder with a specific surface area of 155 m²/g has been prepared using pulsed electron beam evaporation in vacuum. The nanopowder consists of 20- to 500-nm agglomerates formed by crystalline nanoparticles (3–12 nm in diameter) connected by amorphous–nanocrystalline strands. At room temperature, the Gd_2O_3 nanopowder exhibits a paramagnetic behavior. The phase transformations occurring in the powder have been investigated using differential scanning calorimetry and thermogravimetry (40–1400°C). The amorphous phase of the nanopowder is thermally stable up to a temperature of 1080°C. It has been found that the amorphous phase has an inhibitory effect on the temperature of the polymorphic transformation from the cubic phase into the monoclinic phase. It has been revealed that, compared with the microcrystalline powder, the Gd_2O_3 nanopowder is characterized by a complete quenching of photoluminescence.

DOI: 10.1134/S1063783413060127

1. INTRODUCTION

Increased interest in the synthesis of gadolinium oxide (Gd_2O_3) nanoparticles and in the study of their properties is associated with the prospect for the use of these materials in medical diagnostics as multimodal contrast agents in the ultrasound and magnetic resonance imaging (MRI) and computed tomography with the aim of achieving therapeutic effects in radiotherapy and Gd neutron capture therapy of cancer, biomedicine for labeling cells, fluorescence microscopy, microelectronics, and spintronics [1–7].

The dependence of physical properties on the size opens the way for various applications of Gd_2O_3 nanoparticles as protective and corrosive resistant coatings, active additives for the low-temperature synthesis of ceramics, grain growth inhibitors, and phase stabilizers, as well as in optics (antireflective coatings, thin films for ultraviolet lasers), X-ray imaging systems, sensors, nuclear engineering, and other fields of science and technology [8–10].

Currently, the MTI method has most commonly used paramagnetic contrast agents based on gadolinium chelates [11]. However, because of the well-known toxicity of Gd^{3+} ions [12] and recent reports on the development of nephrogenic systemic fibrosis

when using gadolinium chelates [2, 13], it has become more attractive to search for new contrast agents based on biocompatible and inert oxides, for example, oxides of gadolinium, iron, manganese, chromium, etc.

Gadolinium oxide nanoparticles, suitable for the use in the MRI method, have been prepared by different methods, such as the sol–gel method [14], microemulsion method [15], colloidal solution method [16], etc. Moreover, ultrafine Gd_2O_3 particles (1–3 nm in size) have been prepared by the most widely used low-efficient multistage complex method of colloid chemistry—the polyol method [17–19]. In addition, the final stage of the preparation of aqueous suspensions of contrast agents from Gd_2O_3 nanoparticles obtained by the polyol method includes the long-term procedure of the preliminary dialysis. New no-polyol methods of synthesizing Gd_2O_3 nanoparticles are also being developed [20].

Despite the above problems with the preparation of Gd_2O_3 nanoparticles, the investigations of the properties of ultrafine Gd_2O_3 paramagnetic crystals synthesized by the polyol method have demonstrated the prospect of using these materials for preclinical diagnosis of the major types of cancer [21, 22]. In particular, ultrafine Gd_2O_3 nanoparticles with polyethylene

glycol shells have been successfully used for in vivo magnetic resonance imaging of one of the most malignant and poorly studied forms of cancer, namely, GL-261 glioblastoma multiforme.

Choi et al. [16] investigated the longitudinal relaxation of water protons r_1 (r_1 is the parameter of positive magnetic resonance imaging contrast agents) of ultrafine oxide nanoparticles (1–3 nm in size) based on $3d$ and $4f$ transition metals (Fe^{3+}, Mn^{2+}, Eu^{3+}, Gd^{3+}, Dy^{3+}). It was shown experimentally [16] that only ultrafine nanoparticles of iron, manganese, and gadolinium oxides exhibit a significant r_1-relaxation. Moreover, ultrafine Gd_2O_3 nanoparticles (1.5 nm in diameter) are characterized by a record r_1-relaxation (12 mM^{-1} s^{-1}), which is significantly higher than the r_1-relaxation of traditional molecular Gd^{3+} complexes (3–5 mM^{-1} s^{-1}), and the ratio of the spin–spin relaxation r_2 to the longitudinal spin relaxation r_1 near the Gd_2O_3 nanoparticles is $r_2/r_1 \longrightarrow 1$, which corresponds to the ideal ratio for positive contrast agents in the MRI method.

For the purpose to decrease the toxicity of Gd_2O_3 nanoparticles and their aggregation in aqueous suspensions, as well as to enhance contrasting properties, extensive investigations have been performed on Gd_2O_3 nanoparticles covered with shells of various organic (polyethylene glycol [23], dextran [24], polysiloxane [25], diethylene glycol [26]) and inorganic (Gd_2O_3/SiO_2 [15]) substances. In particular, McDonald and Watkin [27] observed that small Gd_2O_3 nanoparticles encapsulated in spherical albumin particles provided a better contrast than free Gd_2O_3 particles and, in strong magnetic fields, retained their contrasting properties despite the observations of weakening these properties in other contrast agents [28].

At room temperature, the paramagnetic state is typical of Gd_2O_3 nanoparticles [16, 29, 30]. However, composite nanoparticles based on Gd_2O_3 exhibit various magnetic properties.

For example, superparamagnetic hollow and paramagnetic mesoporous spherical Gd_2O_3 nanoparticles with a diameter of less than 200 nm, which were synthesized by the sol–gel process and deposition of a precursor upon evaporation of the solvent onto the gelatin template [14], demonstrated a good rate of relaxation at low Gd concentrations and a low toxicity. The superparamagnetism discovered in hollow Gd_2O_3 nanospheres was related by Huang et al. [14] to the presence of carbone residues on the nanoparticle surface.

Amorphous Gd_2O_3 nanoparticles coated with a SiO_2 shell (microemulsion method [15]) are characterized by a ferromagnetic behavior at room temperature (the hysteresis loop parameters are as follows: the saturation magnetization in a magnetic field of ± 10 kOe is 0.28 emu/g, and the coercivity is 70 $\pm$ 5 Oe). The ferromagnetic properties of core–shell Gd_2O_3/SiO_2 structures suggest a possibility of forming ferromagnetic layers at the interface in layered structures from the aforementioned oxides and a perspective of their use in spintronic devices.

The results obtained by Drbohlavova et al. [15] have partially allowed us to hope on the detection of ferromagnetic properties at room temperature (the so-called d^0-ferromagnetism [31]) in undoped Gd_2O_3 nanoparticles when using such a highly nonequilibrium method for synthesizing nanoparticles as pulsed electron beam evaporation.

The experimental detection of d^0-ferromagnetism in thin films of hafnium oxide HfO_2 [32] and in nanoparticles of a number of oxides (CeO_2, Al_2O_3, In_2O_3, SnO_2 [33], ZnO [34], ZrO_2 [35]) increased our interest in the study of the magnetic properties of Gd_2O_3 nanoparticles obtained by pulsed electron beam evaporation. According to Sundaresan et al. [33], the origin of ferromagnetism in inorganic nanoparticles can be associated with the exchange interactions between localized electron spin moments resulting from oxygen vacancies on the surfaces of nanoparticles; moreover, it was suggested that this type of ferromagnetism is caused by surface defects and is a universal characteristic of any inorganic nanoparticles.

At present, it has been well established that there is a correlation of ferromagnetism in undoped oxides with their low crystalline quality, grain boundaries, stresses, and nonequilibrium point defects (oxygen vacancies, interstitial defects, cation vacancies, etc.) [36].

The discovery of d^0-ferromagnetism has changed the point of view of many researchers on the role of dopants, namely, magnetic $3d$ metals, in the formation of ferromagnetism in semiconducting and insulating oxides [33, 37–40]. In particular, Sundaresan et al. [33] and Tietze et al. [39] have argued that defects in oxides are responsible for the origin of magnetism. Straumal et al. [40] revealed a correlation between the magnetization and the volume of grain boundaries in undoped and Mn-doped zinc oxides. In some works, it has been shown [36, 41] that the origin of ferromagnetism can be associated with the film–substrate interface and the developed surface. In a number of studies [35, 36, 42], the authors observed reversible ferromagnetic–diamagnetic–ferromagnetic transformations due to the annealing of micro- and nanometer-sized oxide particles in the reduction and oxidation media. It is obvious that the violation of the stoichiometry due to the formation of vacancies in the oxygen sublattice is one of the major causes for the appearance of ferromagnetism at room temperature in oxides annealed under vacuum [43].

Therefore, it was of interest to investigate the magnetic properties at room temperature in Gd_2O_3 nanoparticles produced by pulsed electron beam evaporation [44]. The high temperature of the evaporated nanoparticles (the temperature in the evaporation

Intensity, arb, units
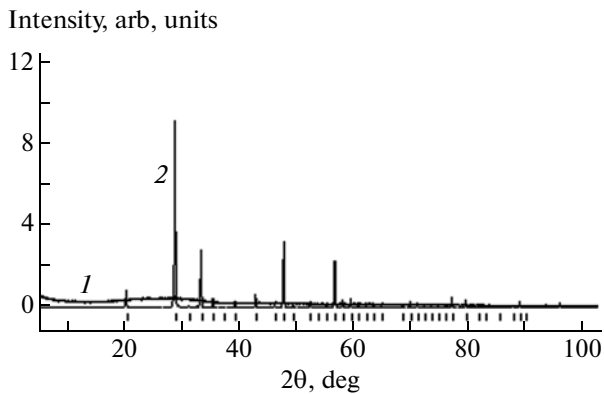
Fig. 1. X-ray diffraction patterns of the Gd_2O_3 nanopowder sample (*1*) before and (*2*) after annealing in air (1100°C).

zone at the target surface is $(5-6) \times 10^{3}°C)$ and their rapid quenching during the deposition on a cold glass substrate make it possible to obtain amorphous Gd_2O_3 nanoparticles whose properties have not been adequately investigated. It was interesting to elucidate the influence of Fe impurities on the magnetic properties of Gd_2O_3 nanoparticles from the viewpoint of the authors of [33, 37–40].

The purpose of this work was to obtain Gd_2O_3 nanoparticles by means of pulsed electron beam evaporation and to investigate their structural, magnetic, and luminescent properties in order to evaluate the possibilities for further applications of nanoparticles as contrast agents in the MRI method.

2. SAMPLE PREPARATION AND EXPERIMENTAL TECHNIQUE

Nanopowders of gadolinium oxide Gd_2O_3 were prepared by sputtering of ceramic targets in a vacuum (at a residual pressure of 4 Pa) using pulsed electron beam evaporation on the NANOBIM-2 installation [44]. Targets in the form of round disks with a diameter of 60 mm and a height of 20 mm were obtained by sintering of pressed pellets from a micron powder of gadolinium(III) oxide (99.9% Gd) (REO, China) in air at a temperature of 1100°C for 1 h. In accordance with the certificate, the content of impurities of rare-earth oxides in the powder was less than 50 ppm, and the iron content was less than 6 ppm.

The electron energy was 40 keV, the electron beam pulse energy was 1.8 J, the pulse duration was 100 μs, and the pulse repetition rate was 100–200 Hz. The deposition of nanoparticles was performed on 4-mm-thick window glass substrates with a large surface area, which were arranged around the target.

The properties of the nanopowders were investigated using the following methods of diagnostics. The chemical analysis was carried out using the inductively coupled plasma (ICP) method on an iCAP 6300 Duo spectrometer and atomic absorption spectroscopy (AAS) on a Perkin-Elmer spectrometer. The specific surface area of the powder (S_{ssa}) was determined by the Brunauer–Emmett–Taylor (BET) method on a Micromeritics TriStar 3000 gas adsorption analyzer after degassing of the test material in a vacuum at a temperature of 300°C for 1 h. The X-ray powder diffraction (XRD) analysis was performed on a Shimadzu XRD 7000 (Japan) diffractometer. The microscopic analysis of the nanopowders was carried out on a JEOL JEM 2100 transmission electron microscope. The magnetic measurements were made on a Cryogenic CFS-9T-CVTI vibrating-sample magnetometer at a temperature of 300 K and in magnetic fields of ±1 T. The thermal analysis the Gd_2O_3 nanopowder was performed on a NETZSCH STA-409 thermal analyzer using thermogravimetry (TG) and differential scanning calorimetry (DSC). The photoluminescence spectra were recorded on an MDR-204 monochromator. The IR spectra were measured on a Perkin-Elmer Spectrum One FT-IR spectrometer (powders suspended in vaseline oil) in the frequency range 400–1000 cm^{-1}.

3. RESULTS AND DISCUSSION

The Gd_2O_3 nanopowder obtained by pulsed electron beam evaporation for 1 h in a vacuum was white in color with a grayish tinge. The specific surface area S_{ssa} of the nanopowder was 155 m^2/g. This value is considerably larger than the value of S_{ssa} for the crystalline nanopowder (15.6 m^2/g) consisting of quasi-spherical nanoparticles with an average size of 54 nm, which was obtained by continuous electron beam evaporation [45] at atmospheric pressure. The nanoparticle size calculated according to the formula $d_{BET} = 6/\rho S_{ssa}$ in the spherical particle shape approximation (for the Gd_2O_3 density $\rho = 7.618$ g/cm^3) was ~5 nm. The contents of magnetic iron impurities in

Fig. 2. TEM and HR TEM images of Gd_2O_3 nanopowders: (a) "foam-like" agglomerate of spherical nanoparticles (with a diameter of 3–12 nm) connected by strands of arbitrary shape; (b) typical agglomerate of Gd_2O_3 nanopowders (framed region of the agglomerate is shown in panel (a)); (c) Gd_2O_3 nanopowder obtained by evaporation with a continuous electron beam [45]; (d) structures in Gd_2O_3 nanopowders with a crystalline core and an amorphous shell (indicated by lines), insets show the electron diffraction patterns of the amorphous (left) and crystalline (right) parts of the sample; (e) morphology of strands in Gd_2O_3 nanopowders with alternating crystalline (*C*) and amorphous (*A*) parts along the strand length; and (f) different defects of crystalline nanoparticles (circles).
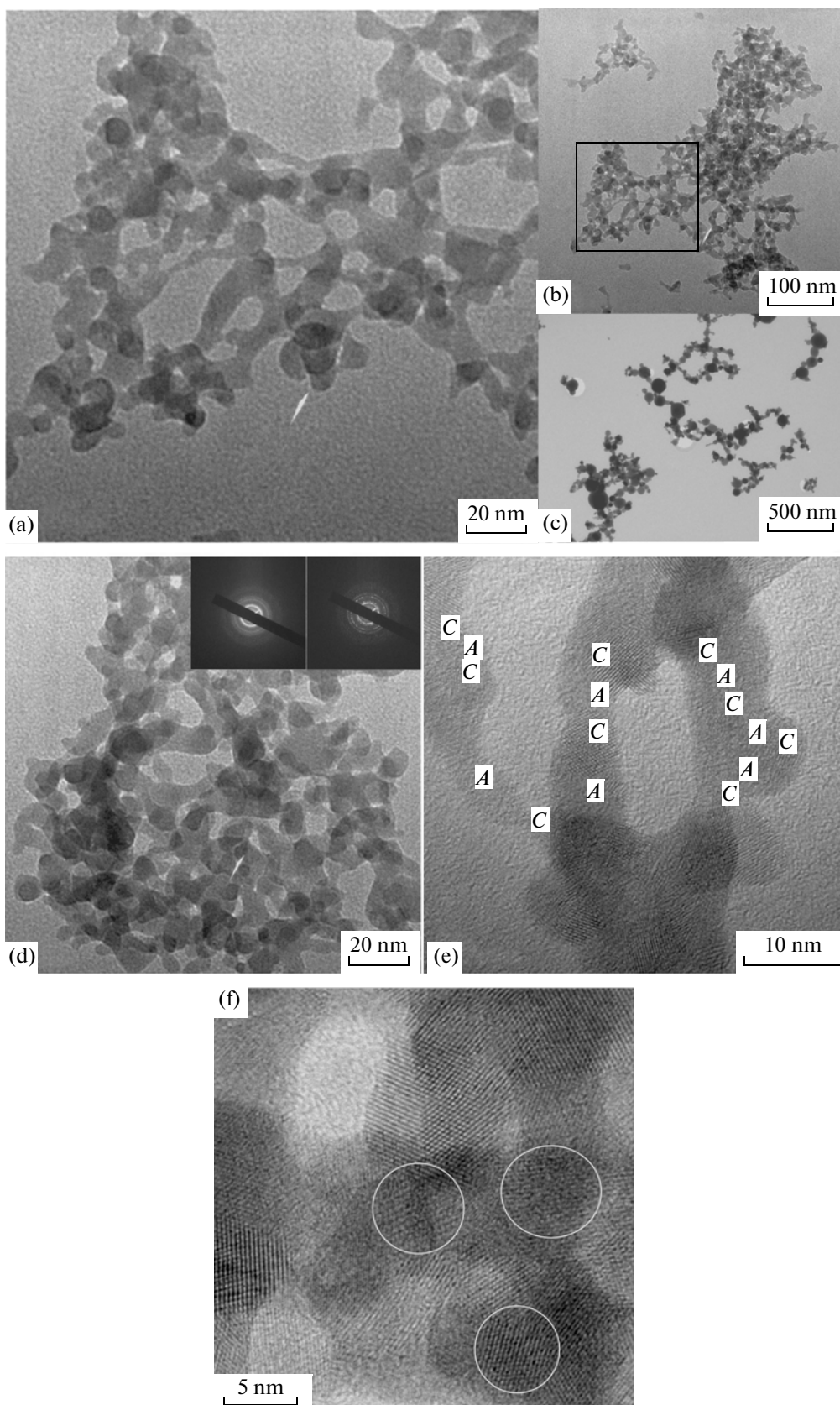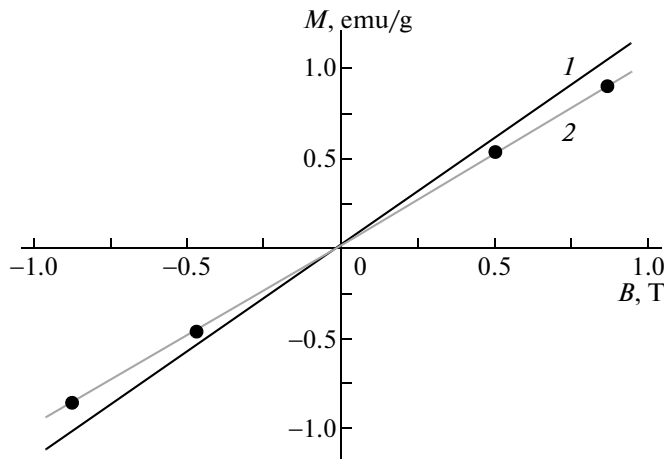
Fig. 3. Dependences of the magnetization of (*1*) Gd_2O_3 microcrystalline powder and (*2*) Gd_2O_3 nanocrystalline powder on the magnetic field in the range ±1 T.

the nanopowder, according to the ICP and AAS data, were less than 0.02 and 0.01 wt %, respectively.

The X-ray diffraction patterns of the Gd_2O_3 nanopowder samples before and after annealing in air at a temperature of 1100°C for 1 h are shown in Fig. 1. After annealing, the nanopowder became bright white in color and markedly decreased in volume.

Before annealing (Fig. 1, curve *1*), the sample was X-ray amorphous (with a crystallinity of less than 5%). After annealing (Fig. 1, curve *2*), the sample became entirely crystalline. The annealed powder had a cubic crystal lattice with the unit cell parameter $a = 10.8269 \pm 9$ Å (calculated from 15 independent lines at angles $2\theta = 60°{-}90°$). We note a small increase in the unit cell parameter of the annealed sample as compared to the reference sample ($a = 10.814$ Å, Card 10-797 JCPDS), which indicates a partial preservation of the lattice strain of Gd_2O_3 after annealing.

Figure 2 shows the transmission electron microscopy images of the Gd_2O_3 nanopowder with low resolution (TEM) and high resolution (HR TEM). The overall morphological pattern of the Gd_2O_3 nanopowder is typical of the majority of oxide nanopowders produced by pulsed electron beam evaporation. The

Static magnetic susceptibility χ of nanocrystalline and microcrystalline powders of Gd_2O_3

Sample	χ, 10^{-4} cm³/g
Microcrystalline Gd_2O_3 powder (annealing, 1100°C, 1 h)	1.494
Amorphous−nanocrystalline Gd_2O_3 powder	
Gd_2O_3	1.286
Data [47]	1.468

nanopowder consists of agglomerates with sizes ranging from 20 to 500 nm (Figs. 2a, 2b). The "foam-like" agglomerate shown in Fig. 2a (and framed in Fig. 2b) contains crystalline spherical nanoparticles with a diameter of approximately 3−12 nm. Spherical nanoparticles are connected by strands (bridges) of arbitrary shape and length. It should be noted that the Gd_2O_3 nanopowder obtained by continuous electron beam evaporation at atmospheric pressure (Fig. 2c [45]) has a morphological pattern (including chains of spherical nanoparticles with sizes up to 200 nm and an average nanoparticle size of 54 nm) similar to that of our nanopowder. However, spherical nanoparticles obtained in [45] do not form extended strands as in our case.

The examination of the structure of strands (bridges) in Gd_2O_3 nanopowders has revealed that the strands are chains consisting of smaller sized nanocrystals (with a diameter of ~3−7 nm) connected by amorphous bridges with a clearly observed periodicity in alternation of crystalline (*C*) and amorphous (*A*) regions throughout the entire strand length (Fig. 2e). Individual agglomerates (Fig. 2d) contain a significant number of core−shell nanoparticles (with a crystalline core and an amorphous shell). The thickness of the shells varies in the range ~2−5 nm, and the total size of the core−shell structures (~12−20 nm) is somewhat larger than that of nanoparticles without shells. In many of the core−shell nanoparticles, the crystalline core is incompletely covered by the amorphous shell. The Gd_2O_3 nanoparticles also contain a large number of structural defects of different types (twins, lattice distortions, point defects, etc.), as can be seen from Fig. 2f.

Thus, the electron microscopic investigations have demonstrated that the Gd_2O_3 nanopowder is not purely amorphous, as was shown by the X-ray diffraction analysis, but, it is actually an amorphous−nanocrystalline powder. The absence of reflections in the X-ray diffraction pattern of the Gd_2O_3 nanopowder (Fig. 1, curve *1*) is not surprising, because it is known [46] that, when the size of Gd_2O_3 nanoparticles is less than 5 nm, no reflections from crystalline phases in X-ray diffraction patterns are observed.

Significantly, the investigation of the influence exerted by the aggregation of Gd_2O_3 nanopowders on their contrasting properties (MRI) showed [22] that the aggregation does not significantly decrease the parameters of the contrast. This also gives hope for the successful application of our nanopowders as contrast agents in the MRI method, especially since there is a possibility to disaggregate the nanopowders with the use of different polymeric shells on the surface of the nanoparticles. In addition, the high porosity of the agglomerates of Gd_2O_3 nanopowders can be used for drug delivery through filling the pores.

The dependences of the magnetization of the Gd_2O_3 nanopowder and the Gd_2O_3 microcrystalline

powder (charge) on the magnetic field in the range ±1 T are shown in Fig. 3.

The powders were characterized by a paramagnetic behavior. The calculated values of the static magnetic susceptibility χ of the initial and nanometer-sized samples are presented in the table. The magnetic susceptibility of the microcrystalline sample is in satisfactory agreement with the reference data. As compared with the initial powder, the nanopowder has a lower value of the magnetization (susceptibility). The magnetization as a function of the magnetic field in both cases is a strictly linear function, which indicates the absence of magnetic order in the samples. It is known that a change in the type of structural order is inevitably reflected in the character of the intramolecular electrostatic field (the Weiss field) and the exchange interaction; therefore, the observed difference (decrease) between the magnetization of the amorphous nanopowder and the value typical of the microcrystalline powder is quite expected. The changes in the magnetization of the nanoparticles can also be caused by the influence of the size factor and surface effects.

Thus, the magnetic measurements have demonstrated that the Gd$_2$O$_3$ nanoparticles produced by pulsed electron beam evaporation do not exhibit d^0-ferromagnetism. However, this observation does not refute the suggestion made by Sundaresan et al. [33] regarding the universality of ferromagnetism at room temperature in inorganic nanoparticles in the presence of oxygen vacancies on the nanoparticle surfaces. As will be shown below (TG analysis data), the concentration of oxygen vacancies in the Gd$_2$O$_3$ nanopowder obtained by pulsed electron beam evaporation is extremely low. This is confirmed by the fact that, in the TG curve measured during the dynamic heating to a temperature of 1400°C, there is no increase in the mass of the nanopowder. In the presence of oxygen vacancies on the surface of nanoparticles, the reverse picture should be observed, i.e., an increase in the mass of the sample. It should be noted that, in the Gd$_2$O$_3$ nanopowder, despite the negligible content of oxygen vacancies, there is a significant number of defects that have a different nature (Fig. 2d), but, which, however, did not lead to the appearance of a ferromagnetic response in the nanopowder. The large number of core−shell nanoparticles and interlayers of the amorphous phase in the nanopowder (Figs. 2b, 2c) also did not induce a ferromagnetic response. Therefore, the absence of d^0-ferromagnetism in the Gd$_2$O$_3$ nanoparticles indicates an extremely important role of oxygen vacancies in the formation of ferromagnetism at room temperature in inorganic nanoparticles in the complete agreement with the hypothesis advanced in [33].

It is worth noting that, in the previously studied nanopowders of ZnO, ZnO−Zn, ZnO−Cu [48, 49], CeO$_2$, CeO$_2$−Cu, CeO$_2$−C [50], Al$_2$O$_3$, Al$_2$O$_3$−Al, Al$_2$O$_3$−Cu [51], ZrO$_2$−Y$_2$O$_3$ [52], ZnS, ZnS−Al [53], in which the content of magnetic Fe impurities
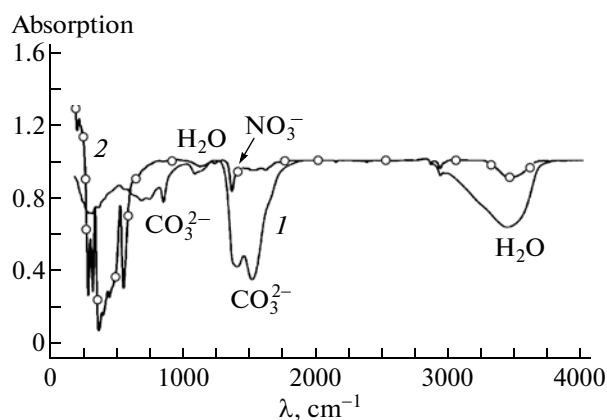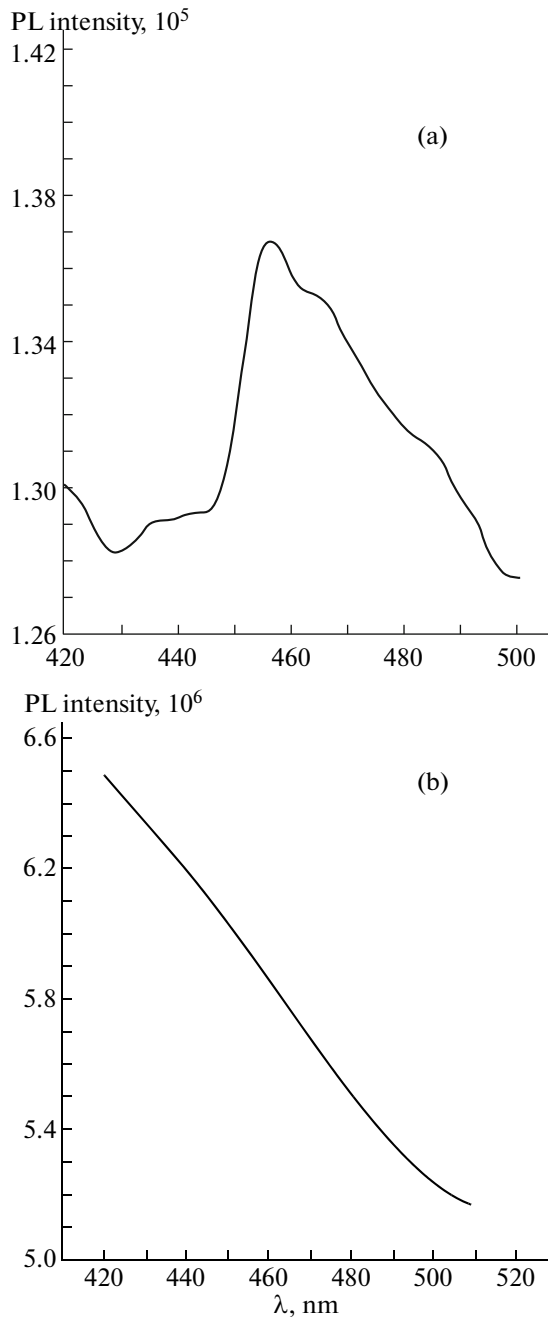

Fig. 4. IR spectra of (*1*) Gd$_2$O$_3$ nanocrystalline powder and (*2*) Gd$_2$O$_3$ microcrystalline powder.

($\leq 10^{-2}$ wt %) was comparable to the Fe content in the Gd$_2$O$_3$ nanopowder (12×10^{-2} wt %), we revealed a significant ferromagnetic response. In contrast to the Gd$_2$O$_3$ nanopowder, the majority of the aforementioned nanopowders contained oxygen vacancies, which was confirmed by the increase in the mass of the sample (TG analysis in air).

Figure 4 shows the IR spectra of the amorphous nanopowder and microcrystalline powder (charge) of Gd$_2$O$_3$. The investigation of the optical properties of the Gd$_2$O$_3$ nanopowder has revealed the following features. In the IR spectrum of the Gd$_2$O$_3$ nanopowder, there are broadened bands, because the nanopowder adsorbed water and carbon compounds. The band at 545 cm^{-1}, which corresponds to the Gd−O bond vibrations, almost completely disappeared. The intrinsic emission from the Gd$_2$O$_3$ powder target represents a broad spectrum with the maximum at a wavelength of ~456.34 nm. The emission is caused by charge transfer in Gd polyhedra. The separate peaks observed in the emission curve with flat maxima are probably attributed to the electron−vibration interactions in the Gd polyhedra.

The photoluminescence spectra of the amorphous nanopowder and microcrystalline powder (charge) of Gd$_2$O$_3$ are shown in Fig. 5. It can be seen from this figure that there is no intrinsic luminescence of the Gd$_2$O$_3$ nanopowder in the excitation region 220–300 nm (λ_{ex}^{max}), which is probably due to the change of chemical bonds in the Gd polyhedra. At the same time, there is a complete quenching of the luminescence of the nanopowder at the wavelength $\lambda_{max} = 456$ nm, which is probably caused by the significant difference between the equilibrium Gd−O distances in the microcrystalline and nanocrystalline powders. In the framework of the configuration−coordination model, this difference is responsible for the nonradiative return of the optical centers to the ground state.

PL intensity, 10^5

PL intensity, 10^6

Fig. 5. Photoluminescence spectra of (a) microcrystalline powder and (b) amorphous–nanocrystalline powder of Gd_2O_3.

It should be noted that the study of fluorescence of the ceramics (grain size 20–25 μm) sintered from the crystalline Gd_2O_3 nanopowder obtained by continuous electron beam evaporation [45] also showed that the radiation with a wavelength of 248 nm excites in the Gd_2O_3 ceramics only a weak reddish luminescence that is insufficient to observe the fluorescence spectrum.

After isothermal annealing in air at a temperature of 1100°C for 1 h, as was shown above (Fig. 1), the amorphous Gd_2O_3 nanopowder completely transformed into the cubic phase, which is well consistent with the data reported in [54] on the formation of a cubic phase due to the isothermal annealing (at 1000°C for 6–7 h, at 1300°C for 1–2 h).

Figure 6 shows the DSC–TG heating/cooling thermograms of the Gd_2O_3 nanopowder measured in the temperature range 40–1400°C in air.

The heating/cooling rate of the sample was 10°C/min. It can be seen that, in the DSC heating curve, there are four thermal peaks (denoted by numerals *1–4* in Fig. 6). Endothermic peak *1* at low temperatures is caused by the evaporation of adsorbed water from the surface of the nanopowder. The mass spectrum of H_2O and kink I in the TG curve indicate that the evaporation of the greater part of H_2O molecules occurs during heating of the sample to a temperature of ~230°C. Extended exothermic peak *2* in the temperature range 230–1025°C is caused by the annealing of unknown carbon compounds adsorbed on the developed surface of the nanopowder. The main part of the organic molecules is removed from the sample by heating to a temperature of approximately 800°C. This is indicated by the sharp decrease in the mass of the sample (kink II in the TG curve in the temperature range 230–800°C) and the mass spectrum of CO_2. The carbon molecules completely evaporate from the sample during heating to a temperature of approximately 1080°C, which is consistent with the data presented in [55], where the removal of organic compounds was observed upon heating the Gd_2O_3 nanopowder to a temperature of 1000°C.

The crystallization of the amorphous phase of the nanopowder begins with the temperature of approximately 1080°C (exothermic peak *3* in the DSC curve) and ends at the temperature of approximately 1300°C. The heat contribution from the crystallization of the amorphous phase to the Gd_2O_3 cubic phase is found to be rather large (160.3 kJ/mol). It should be noted that the transformation of the amorphous phase of the Gd_2O_3 nanopowder (sol–gel method [55]) into the cubic phase was observed at a lower temperature of 650°C. This confirms that the phase transformations in rare-earth oxides depend on the method used for their preparation.

Exothermic peak *4* on the DSC curve at 1300°C corresponds to the polymorphic transformation from the Gd_2O_3 cubic phase (*C*) into the monoclinic phase (*B*) and agrees with the data available in the literature, according which this polymorphic transformation occurs with the heat release [54]. In this case, the equilibrium temperature of the polymorphic transformation is slightly lower and equal to 1152°C (1425 K) [56]. The enthalpy of the phase transformation $C \longrightarrow B$ in the sample is equal to 75.6 kJ/mol and significantly (by an order of magnitude) exceeds the corresponding enthalpy for the bulk sample of Gd_2O_3
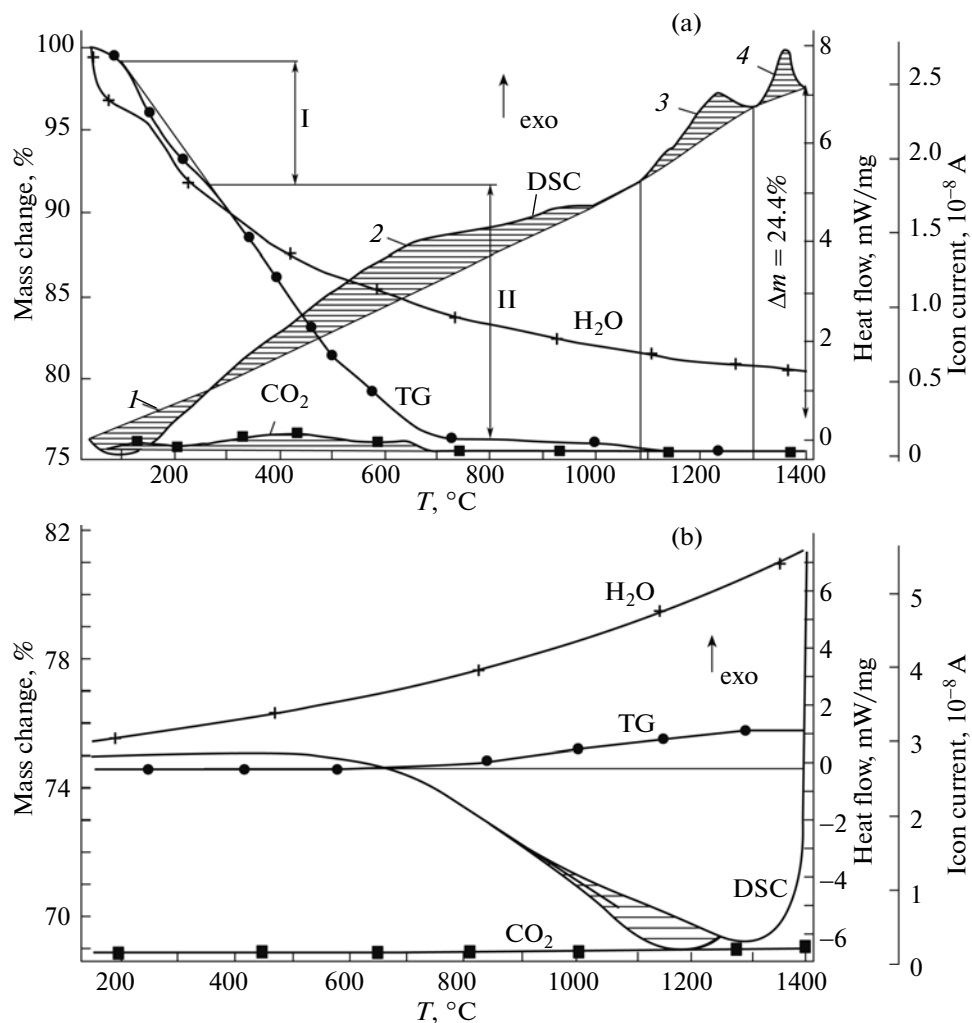
Fig. 6. DSC–TG curves of (a) heating and (b) cooling and mass spectra of H$_2$O and CO$_2$ in the temperature range 40–1400°C of the amorphous–nanocrystalline Gd$_2$O$_3$ powder.

(5.3 kJ/mol at T = 1561 K), which was measured by the DSC method in [57]. We also note a nearly twofold excess of the heat release in the crystallization of the amorphous phase (160.3 kJ/mol) as compared to the enthalpy of the phase transition $C \longrightarrow B$ (75.6 kJ/mol). The increased heat release in the crystallization of the amorphous phase and in the phase transition $C \longrightarrow B$, as compared to the corresponding equilibrium parameters [56], can be explained by the influence of the size factor. The effect of significant energy storage by nanoparticles was demonstrated in [58, 59]. An increase in the temperature of the transformation $C \longrightarrow B$ to 1300°C during the phase transformation of the amorphous nanopowder with respect to the equilibrium transformation temperature (1152°C) [56] is most likely caused by the inhibitory effect of the amorphous phase on the transformation temperature.

It can be seen from the DSC cooling curve (Fig. 6b) that the phase transformation $C \longrightarrow B$ is reversible, which is indicated by the intense endothermic peak

observed at approximately 1250°C in the reaction $B \longrightarrow C$. A slight supercooling of the sample (by ~50°C) is most likely caused by the high cooling rate of the sample (10°C/min) and the slow kinetics of the polymorphic transformation $B \longrightarrow C$; therefore, the temperature of 1250°C cannot be used to determine the onset temperature of the transformation $B \longrightarrow C$.

The heating to a temperature of 1400°C (the TG curve in Fig. 6a) leads to a significant decrease in the mass of the sample (24.4%) due to the evaporation of water and organic carbon from the surface of Gd$_2$O$_3$ nanoparticles. The adsorption of water and organic molecules on the surface of Gd$_2$O$_3$ nanoparticles could occur both directly during the deposition of nanoparticles in the evaporation chamber because of the high residual pressure (4 Pa) and after the removal of the sample from the chamber due to the capture of water vapors and organic molecules from the surrounding atmosphere by the highly developed surface

of the nanoparticles. There is an obvious need to create the appropriate conditions for preventing contamination of the material with organic compounds both in the processes of production/extraction of the material and in its further storage.

A continuous decrease in the mass of the sample during heating (the TG curve in Fig. 6a) indicates a low content of oxygen vacancies in amorphous Gd_2O_3; otherwise, the annealing would lead to an increase in the mass of the sample.

Thus, the DSC–TG analysis has revealed that the amorphous phase Gd_2O_3 retains the thermal stability to a sufficiently high temperature ($\sim$1080°C) and completely transforms into the cubic phase at 1300°C. The high thermal stability of the amorphous phase indicates the prospects for its possible use in various high-temperature applications.

4. CONCLUSIONS

An amorphous–nanocrystalline Gd_2O_3 powder with the specific surface area $S_{ssa} = 155$ m²/g has been prepared using pulsed electron beam evaporation in vacuum. According to the IR and mass spectrometry data, significant adsorption of carbon occurs on the developed surface of the nanopowder (the sample loses 24% of the initial mass due to the removal of volatile compounds during heating to 1400°C).

The nanopowder consists of agglomerates ($\sim$20–500 nm in size) formed by perfect spherical nanoparticles (3–12 nm in diameter) connected by amorphous–nanocrystalline strands. The nanopowder contains a large number of structural defects of different types. After isothermal annealing in air for 1 h at a temperature of 1100°C, the nanopowder completely transforms into the Gd_2O_3 cubic phase.

During dynamic heating (DSC) to 1400°C, the amorphous phase in the nanopowder crystallizes (1080°C) into the Gd_2O_3 cubic modification, which then transforms into the monoclinic modification at a temperature of 1300°C. An increase in the temperature of the beginning of the phase transition $C \longrightarrow B$ by $\sim$150°C, as compared with the equilibrium temperature of the transition in the bulk powder, is most likely associated with the inhibitory effect of the amorphous phase on the phase transition temperature. During cooling of the nanopowder, the reverse polymorphic transformation $B \longrightarrow C$ occurs at a temperature of approximately 1250°C.

The magnetic measurements showed that the nanopowder exhibits a paramagnetic behavior typical of bulk Gd_2O_3. A small decrease in the magnetization of the nanopowder, as compared to microparticles, can be explained by the influence of the size effect on the magnetization; no d^0-ferromagnetism in the Gd_2O_3 nanopowder was found. The probable cause for the absence of d^0-ferromagnetism is the low concentration of oxygen vacancies in the nanopowder.

The complete quenching of the photoluminescence in the Gd_2O_3 nanopowder was observed at the wavelength $\lambda_{max} = 456$ nm.

The high thermal stability (1080°C), small sizes (3–12 nm) and paramagnetic properties of Gd_2O_3 nanoparticles, strong adsorption of carbon molecules, and high specific surface area of the nanopowder indicate that the amorphous–nanocrystalline Gd_2O_3 powders obtained by pulsed electron beam evaporation are promising materials for the use as contrast agents in magnetic resonance imaging, acoustic imaging, and Gd neutron capture therapy in medicine, carbon sensors, and many other applications.

REFERENCES

1. J. Y. Park, M. J. Baek, E. S. Choi, S. Woo, J. H. Kim, T. J. Kim, J. C. Jung, K. S. Chae, Y. Chang, and G. H. Lee, ACS Nano **3**, 3663 (2009).

2. P. Sharma, W. G. Brown, S. Santra, E. Scott, H. Ichikawa, Y. Fukumori, and B. M. Moudgil, Adv. Power Technol. **18**, 663 (2007).

3. S. Roux and O. Tillement, Int. J. Nanotechnol. **7**, 781 (2010).

4. M. Engström, A. Klasson, H. Pedersen, C. Vahlberg, P. O. Käll, and K. Uvdal, Magn. Reson. Mater. Phys. Biol. Med. **19**, 180 (2006).

5. A. Klasson, M. Ahren, E. Hellqvist, F. Soderlind, A. Rosen, P. O. Kall, K. Uvdal, and M. Engstrom, Contrast Media Mol. Imaging **3**, 106 (2008).

6. A. Hedlund, M. Ahren, H. Gustafsson, N. Abrikossova, M. Warntjes, J. I. Jonsson, K. Uvdal, and M. Engstrom, Int. J. Nanomed. **6**, 3233 (2011).

7. L. Faucher, M. Tremblay, J. Lagueux, Y. Gossuin, and M. A. Fortin, ACS Appl. Mater. Interfaces **4**, 4506 (2012).

8. H. Y. Chen, C. Y. He, C. X. Gao, J. H. Zhang, S. Y. Gao, H. L. Lu, Y. G. Nie, D. M. Li, S. H. Kan, and G. T. Zou, Chin. Phys. Lett. **24**, 158 (2007).

9. F. X. Zhang, M. Lang, J. W. Wang, U. Becker, and R. C. Ewing, Phys. Rev. B: Condens. Matter. **78**, 064114 (2008).

10. P. K. Jain, X. Huang, I. H. El-Sayed, and M. A. El-Sayed, Acc. Chem. Res. **41**, 1578 (2008).

11. P. Caravan, Chem. Soc. Rev. **35**, 512 (2006).

12. A. Palasz and P. Czekaj, Acta Biochim. Pol. **47**, 1107 (2000).

13. C. Briguori, A. Colombo, F. Airoldi, G. Melzi, I. Michev, M. Carlino, M. Montorfano, A. Chieffo, R. Bellanca, and B. Ricciardelli, Catheterization Cardiovasc. Interventions **67**, 175 (2006).

14. C. C. Huang, T. Y. Liu, C. H. Su, Y. W. Lo, J. H. Chen, and C. S. Yeh, Chem. Mater. **20**, 3840 (2008).

15. J. Drbohlavova, R. Hrdy, V. Adam, R. Kizek, O. Schneeweiss, and J. Hubalek, Sensors **9**, 2352 (2009).

16. E. S. Choi, J. Y. Park, K. Kattel, W. Xu, G. H. Lee, M. J. Baek, J. H. Kim, Y. C. Tae, and J. Kim, J. Korean Phys. Soc. **56**, 1532 (2010).

17. R. Bazzi, M. A. Flores, C. Louis, K. Lebbou, W. Zhang, C. Dujardin, S. Roux, B. Mercier, G. Ledoux, E. Bernstein, P. Perriat, and O. Tillement, J. Colloid Interface Sci. **273**, 191 (2004).

18. R. Bazzi, M. A. Flores-Gonzalez, C. Louis, K. Lebbou, C. Dujardin, A. Brenier, W. Zhang, O. Tillement, E. Bernstein, and P. Perriat, J. Lumin. **102**, 445 (2003).

19. U. Louis, R. Bazzi, C. A. Marquette, J. L. Bridot, S. Roux, G. Ledoux, B. Mercier, L. Blum, P. Perriat, and O. Tillement, Chem. Mater. **17**, 1673 (2005).

20. M. Ahrén, L. Selegård, F. Söderlind, M. Linares, J. Kauczor, P. Norman, P. O. Käll, and K. Uvdal, J. Nanopart. Res. **14**, 1006 (2012).

21. L. Faucher, A. A. Guay-Bégin, J. Lagueux, M. F. Côté, E. Petitclerc, and M. A. Fortin, Contrast Media Mol. Imaging **6**, 209 (2011).

22. L. Faucher, Y. Gossuin, A. Hocq, and M. A. Fortin, Nanotechnology **22**, 295103 (2011).

23. M. A. Fortin, R. M. Petoral, F. Söderlind, A. Klasson, M. Engstrom, T. Veres, P. O. Käll, and K. Uvdal, Nanotechnology **18**, 395501 (2007).

24. M. A. McDonald and K. L. Watkin, Acad. Radiol. **13**, 421 (2006).

25. J. L. Bridot, A. C. Faure, S. Laurent, C. Riviére, C. Billotey, B. Hiba, M. Janier, V. Josserand, J. L. Coll, L. V. Elst, R. Muller, S. Roux, P. Perriat, and O. J. Tillement, J. Am. Chem. Soc. **129**, 5076 (2007).

26. J. L. Bridot, D. Dayde, C. Riviére, C. Mandon, C. Billotey, S. Lerondel, R. Sabattier, G. Cartron, A. Le Pape, G. Blondiaux, M. Janier, P. Perriat, S. Roux, and O. Tillement, J. Mater. Chem. **19**, 2328 (2009).

27. M. A. McDonald and K. L. Watkin, Invest. Radiol. **38**, 305 (2003).

28. R. J. Gillies, *NMR in Physiology and Biomedicine* (Academic, San Diego, 1994).

29. Y. P. Chang, K. H. Liu, C. S. Chao, S. Y. Chen, and D. M. Liu, Acta Biomater. **6**, 3713 (2010).

30. J. C. Paeng and D. S. Lee, Open Nucl. Med. J. **2**, 145 (2010).

31. J. M. D. Coey, Solid State Sci. **7**, 660 (2005).

32. M. Venkatesan, C. B. Fitzgerald, and J. M. D. Coey, Nature (London) **430**, 630 (2004).

33. A. Sundaresan, R. Bhargavi, N. Rangarajan, U. Siddesh, and C. N. R. Rao, Phys. Rev. B: Condens. Matter **74** (16), 161306 (2006).

34. K. Ueda, H. Tabata, and T. Kawai, Appl. Phys. Lett. **79**, 988 (2001).

35. L. S. Panchakarla, Y. Sundarayya, S. Manjunatha, A. Sundaresan, and C. N. R. Rao, Chem. Phys. Chem. **11**, 1673 (2010).

36. S. Mal, T. H. Yang, C. Jin, S. Nori, J. Narayan, and J. T. Prater, Scr. Mater. **65**, 1061 (2011).

37. L. I. Burova, N. S. Perov, A. S. Semisalova, V. A. Kulbachinskii, V. G. Kytin, A. L. Roddatis, V. V. Vasiliev, and A. R. Kaul, Thin Solid Films **520**, 4580 (2012).

38. N. H. Honga, J. Sakaib, and F. Gervaisa, J. Magn. Magn. Mater. **316**, 214 (2007).

39. T. Tietze, M. Gacic, G. Schütz, G. Jakob, S. Brück, and E. Goering, New J. Phys. **10**, 055009 (2008).

40. B. B. Straumal, A. A. Mazilkin, S. G. Protasova, A. A. Myatiev, P. B. Straumal, G. Schütz, P. A. van Aken, E. Goering, and B. Baretzky, Phys. Rev. B: Condens. Matter **79**, 205206 (2009).

41. N. H. Hong, J. Sakai, N. Poirot, and V. Brize, Phys. Rev. B: Condens. Matter **73**, 132404 (2006).

42. D. A. Schwartz and R. Gamelin, Adv. Mater. (Weinheim) **16**, 2115 (2004).

43. P. Karen, J. Solid State Chem. **179**, 3167 (2006).

44. Yu. A. Kotov, S. Yu. Sokovnin, V. G. Il'ves, and C. K. Rhee, RF Patent No. 2 353 573, Byull. Izobret., No. 12 (April 27, 2009).

45. S. P. Bardakhanov, V. I. Lysenko, A. N. Malov, N. A. Maslov, and A. V. Nomoev, Fiz. Mezomekh. **11** (5), 111 (2008).

46. F. Soderlind, Doctoral Thesis, Comprehensive Summary. Linköping Studies in Science and Technology Dissertation (Linköping University, Linköping, Sweden, 2008), No. 1182.

47. *Landolt–Börnstein, Numerical Data and Functional Relationships in Science and Technology* (Springer-Verlag, Heidelberg, 1986–1992).

48. V. G. Il'ves and S. Yu. Sokovnin, Nanotechnol. Russ. **6** (1–2), 137 (2011).

49. S. Yu. Sokovnin, V. G. Il'ves, A. I. Medvedev, A. M. Murzakaev, and M. A. Uimin, in *Proceedings of the IV All-Russian Conference on Nanomaterials, Moscow, March 1–4, 2011* (Institute of Metallurgy and Material Science, Russian Academy of Sciences, Moscow, 2011), p. 128.

50. V. G. Il'ves and S. Yu. Sokovnin, Nanotechnol. Russ. **7** (5–6), 213 (2012)

51. V. G. Il'ves, A. I. Medvedev, A. M. Murzakaev, S. Yu. Sokovnin, A. V. Spirina, M. A. Uimin, Fiz. Khim. Obrab. Mater., No. 2, 65 (2011).

52. S. Yu. Sokovnin and V. G. Il'ves, Tech. Phys. Lett. **35** (11), 1026 (2009).

53. V. G. Il'ves and S. Yu. Sokovnin, in *Problems of Spectroscopy and Spectrometry: Interuniversity Collection of Scientific Works* (Ural State Technical University, Yekaterinburg, 2010), Issue 26, p. 237 [in Russian].

54. A. Jandelli, Gazz. Chim. Ital. **77**, 312 (1947).

55. A. García-Murillo, C. Le Luyer, C. Dujardin, C. Pedrini, and J. Mugnier, Opt. Mater. **16**, 39 (2001).

56. M. Zinkevich, Prog. Mater. Sci. **52**, 4597 (2007).

57. U. Kolitsch, PhD Thesis (University of Stuttgart, Stuttgart, Germany, 1995).

58. A. P. Il'in, L. O. Root, and A. V. Mostovshchikov, Tech. Phys. **57** (8), 1178 (2012).

59. G. V. Ivanov, N. A. Yavorovskii, Yu. A. Kotov, V. I. Davydovich, and G. A. Mel'nikova, Dokl. Akad. Nauk SSSR **275**, 871 (1984).

Translated by O. Borovik-Romanova